Received: 13 October 2020 | Revised: 30 May 2021 | Accepted: 24 July 2021

DOI: 10.1002/mp.15149

RESEARCH ARTICLE

MEDICAL PHYSICS

The impact of MR-based attenuation correction in spinal cord FDG-PET/MR imaging for neurological studies

Valentina Brancato[1] | **Pasquale Borrelli**[1] | **Vincenzo Alfano**[1] | **Marco Picardi**[2] | **Mario Mascalchi**[3] | **Emanuele Nicolai**[1] | **Marco Salvatore**[1] | **Marco Aiello**[1]

[1] IRCCS SDN, Naples, Italy

[2] Department of Clinical Medicine and Surgery, Federico II University Medical School, Naples, Italy

[3] Department of Experimental and Clinical Biomedical Sciences "Mario Serio", University of Florence, Florence, Italy

Correspondence
Marco Aiello, IRCCS SDN, Via E. Gianturco, 113, Naples, 80137, Italy.
Email: marco.aiello@synlab.it

Funding information
"Ricerca Corrente" Grant from Italian Ministry of Health (IRCCS SDN).

Abstract

Purpose: Positron emission tomography (PET) attenuation correction (AC) in positron emission tomography-magnetic resonance (PET/MR) scanners constitutes a critical and barely explored issue in spinal cord investigation, mainly due to the limitations in accounting for highly attenuating bone structures which surround the spinal canal. Our study aims at evaluating the clinical suitability of MR-driven AC (MRAC) for 18-fluorodeoxy-glucose positron emission tomography (^{18}F-FDG-PET) in spinal cord.

Methods: Thirty-six patients, undergoing positron emission tomography-computed tomography (PET/CT) and PET/MR in the same session for oncological examination, were retrospectively analyzed.

For each patient, raw PET data from PET/MR scanner were reconstructed with 4- and 5-class MRAC maps, generated by hybrid PET/MR system (PET_MRAC4 and PET_MRAC5, respectively, where PET_MRAC is PET images reconstructed using MR-based attenuation correction map), and an AC map derived from CT data after a custom co-registration pipeline (PET_rCTAC, where PET_rCTAC is PET images reconstructed using CT-based attenuation correction map), which served as reference. Mean PET standardized uptake values (SUV_m) were extracted from the three reconstructed PET images by regions of interest (ROIs) identified on T2-weighted MRI, in the spinal cord, lumbar cerebrospinal fluid (CSF), and vertebral marrow at five levels (C2, C5, T6, T12, and L3). SUV_m values from PET_MRAC4 and PET_MRAC5 were compared with each other and with the reference by means of paired *t*-test, and correlated using Pearson's correlation (*r*) to assess their consistency. Cohen's *d* was calculated to assess the magnitude of differences between PET images.

Results: SUV_m values from PET_MRAC4 were lower than those from PET_MRAC5 in almost all analyzed ROIs, with a mean difference ranging from 0.03 to 0.26 (statistically significant in the vertebral marrow at C2 and C5, spinal cord at T6 and T2, and CSF at L3). This was also confirmed by the effect size, with highest values at low spinal levels ($d = 0.45$ at T12 in spinal cord, $d = 0.95$ at L3 in CSF). SUV_m values from PET_MRAC4 and PET_MRAC5 showed a very good correlation ($0.81 < r < 0.97$, $p < 0.05$) in all

Abbreviations: AC, attenuation correction; CSF, cerebrospinal fluid; CT, computed tomography; FOV, field of view; LAC, linear attenuation correction coefficient; MR, magnetic resonance; MRAC4, 4-tissues MR-based attenuation correction map; MRAC5, 5-tissues MR-based attenuation correction map; MRI, magnetic resonance imaging; PET, positron emission tomography; PET/MR, positron emission tomography-magnetic resonance; PET_MRAC, PET images reconstructed using MR-based attenuation correction map; PET_rCTAC, PET images reconstructed using CT-based attenuation correction map; rCTAC, CT-based attenuation correction map; ROI, region of interest; SC, spinal cord; SUV, standardized uptake value

spinal ROIs. Underestimation of SUV_m between PET_MRAC4 and PET_rCTAC was observed at each level, with a mean difference ranging from 0.02 to 0.32 (statistically significant in the vertebral marrow at C2 and T6, and CSF at L3). Although PET_MRAC5 underestimates PET_rCTAC (mean difference ranging from 0.02 to 0.3), an overall decrease in effect size could be observed for PET_MRAC5, mainly at lower spinal levels (T12, L3). SUV_m from both PET_MRAC4 and PET_MRAC5 methods showed r value from good to very good with respect to PET_rCTAC ($0.67 < r < 0.9$ and $0.73 < r < 0.94$, $p < 0.05$, respectively).

Conclusions: Our results showed that neglecting bones in AC can underestimate the FDG uptake measurement of the spinal cord. The inclusion of bones in MRAC is far from negligible and improves the AC in spinal cord, mainly at low spinal levels. Therefore, care must be taken in the spinal canal region, and the use of AC map reconstruction methods accounting for bone structures could be beneficial.

KEYWORDS
attenuation correction, multimodal coregistration, PET/MR, spinal cord

1 | INTRODUCTION

The integrated positron emission tomography-magnetic resonance (PET/MR) scanner is a powerful diagnostic tool which allows to achieve, in one shot, both metabolic information provided by PET imaging and functional and morphological information with excellent soft tissue contrast provided by magnetic resonance imaging (MRI), together with the substantial reduction in terms of radiation dose received by patients in comparison with positron emission tomography-computed tomography (PET/CT).

PET/MR offers intrinsic alignment of anatomical or functional MRI data with molecular PET information. The well-known high soft tissue contrast obtained with MRI provides more precise information on tumor localization and spread thus increasing the delineation accuracy of target volumes, also in radiotherapy planning.[1,2] The number of studies evaluating clinical applications of hybrid PET/MR is rapidly increasing also in the field of neurological applications, including neuro-oncology, epilepsy, dementia, cerebrovascular disease, and psychiatric and neurological research.[3,4] In this context, due to the frequent involvement of the spinal cord in neurological diseases,[5–7] addition of spinal cord metabolic information to brain imaging might improve the informative potential of PET on the specific pathophysiological mechanisms.[7]

Despite the progress made during the last decade, some relevant issues remain in PET attenuation correction (AC) procedures for integrated PET/MR scanners, especially in whole-body imaging.[8,9] This is due to the lack of a direct relationship between MRI signal intensities (based on proton density and relaxation times) and the 511 keV linear AC coefficients (LACs), which are associated with photon attenuation properties of biological tissues. Conversely, it is well-known that, in PET/CT applications, the conversion of Hounsfield units to 511 keV LACs can be performed through a piece-wise linear transformation suitable for clinical purposes.[10] This is the reason why CT-based AC (CTAC) is currently accepted as reference for AC of PET data. However, given the potential of PET/MR for clinical and research purposes, efforts are being made to reduce inaccuracies of AC methods derived from PET/MR aiming at demonstrating the benefits of this technology in whole-body applications. The clinical suitability of the current implemented AC techniques on commercial PET/MR scanners, especially for whole-body applications, continues to be a matter of intense debate, as evidenced by Catana et al.[9] Indeed, as reported in the previously cited work,[9] although the aforementioned technical issues can be viewed as the main obstacle for the clinical suitability of PET/MR, on the other hand opposite statements highlight on the increased performance of current commercially available AC techniques for PET/MR scanners thus considering them substantially acceptable for clinical purposes.

Among the variety of proposed MR-based AC (MRAC) methods for whole-body applications, the most commonly used is the so-called *baseline segmentation method*, which is implemented on the Siemens Biograph mMR (Erlangen). With the latter method, the AC is performed using the MR data acquired with a two-point Dixon volume interpolated breath-hold examination MR sequence.[8] In-phase, out-of-phase, water, and fat images are generated at each bed position and combined to generate the corresponding whole-body images. First, thresholds are placed on in-phase images in order to separate the voxels corresponding to the subject from the background air. An atlas-based approach is next used to segment the lungs. Then, the

voxels corresponding to fat and soft tissue are obtained from the fat and water images, and an additional post-processing is performed to remove the skin voxels and noise. Finally, four classes (background air, lung, fat, and soft tissue) are segmented, and predefined LACs (0, 0.022, 0.085, and 0.100 cm^{-1}, respectively) are assigned to generate the attenuation map (MRAC4). Notably, the bone tissue is misclassified as soft tissue.[11]

The limitation in accounting for high attenuation structures such as bones has been shown to produce large PET image bias,[8,12] and this poses a considerable challenge for PET/MR investigations of the spinal cord, which is surrounded by dense bony structures. Recently, PET/MR scanners implemented a five-compartment segmentation model based on Dixon, introduced by Paulus et al.[13] According to this model, continuous bone LACs (ranging from 0.1 to 0.2485 cm^{-1}) were superimposed on MRAC map by co-registration of the Dixon series to an atlas of MR and CT pairs of the major bones (skull, spine, pelvis, and proximal femurs) in the body, resulting in a five-tissues MRAC (MRAC5) map.

Extensive literature exists on the impact of MRAC approaches on brain applications,[14–17] while a limited number of studies were performed on whole-body MRAC probably reflecting the greater inter-subject anatomical variability, physiological (respiratory and cardiac) and nonphysiological subject's movement.[12] In addition, the difficulty to image bone structures should be considered due to the short T2* relaxation time of bone tissue, which makes it hardly differentiable in MR images.[18,19] The lower percentage of bone tissue in body than in the head makes the "missing bone" MRAC4 methods reliable for many whole-body clinical applications.[11,12,20,21] In this context, several studies compared the "missing-bone" PET/MR AC with the most commonly used piece-wise linear AC method implemented in PET/CT scanners for whole-body applications by evaluating the uptake in different body tissues including bony structures and regions surrounding them,[11,22–26] and the impact of bone tissue on standardized uptake values (SUV) quantification in other tissues.[27,28] In particular, considerable underestimation in SUVs was found when using MRAC4 with respect to CTAC, particularly in bone lesions or regions surrounding bones.[11,12,22,23,29,30] Few recent studies[13,31–33] investigated the impact of MRAC5 in whole-body PET/MR evaluation, and none of them was specific for spinal zone. Given the substantial amount of bone surrounding spinal zone, PET/MR studies specifically addressing spine and spinal cord MRAC are desirable.

To our knowledge, the impact of MRAC on whole-body PET images, focusing on bone marrow and spinal cord, has been poorly investigated.

Keereman et al.[34] investigated the influence of the MRAC4 in whole-body PET acquisition of phantom data by analyzing different regions, including the spine. In the study proposed by Samarin et al.,[30] the impact of a simulated MRAC4 map on SUV values was evaluated with respect to results obtained with the reference CTAC map within spine lesions. With a similar approach, Kim et al.[35] also started from a simulated MRAC4 map by applying different segmentation techniques to the CT image in order to compare the obtained SUV values in spine lesions with respect to SUV values from CTAC map.

Due to the need for accurate bone segmentation in MRAC for whole-body PET/MR imaging, the aim of the present work was to compare 18-fluorodeoxy-glucose positron emission tomography (^{18}F-FDG-PET) data corrected with PET MRAC map (both with MRAC4 and MRAC5) provided by the hybrid PET/MR system with respect to those corrected with AC maps derived from CT image (rCTAC, CT-based attenuation correction map), for spine and spinal cord studies. In particular, given the intention of investigating PET/MR imaging for neurological studies of spinal cord, our investigation was on oncologic patients without evidence of lesions within the spine and the spinal cord. The rCTAC map is adopted in the study since it can be considered as the reference for bone LAC values due to accuracy of CT in imaging compact bone structures. Moreover, we also aimed at investigating the effect of including bone in Dixon-based AC for PET/MRI of spinal area by comparing both MRAC segmentation models.

2 | MATERIALS AND METHODS

2.1 | Patient characteristics

Data were retrospectively selected from subjects who underwent PET/MR for oncological staging and showed normal spine and spinal cord.

Thirty-six patients who underwent PET/CT and PET/MR in the same session were retrospectively selected. Patient population included 18 men and 18 women, with a mean age of 48.2 ± 18.3 years.

2.2 | PET/CT acquisition

Data were acquired after 6 h of fasting prior to scan; body weight, height, and glucose levels were measured. After the intravenous injection of FDG (350-370 MBq), patients took a rest for 45 min. During the acquisition, patients lied down supine in the PET/CT scanner, with their arms up and eyes closed. The head was placed naturally so that the patient was comfortable, and motion could be minimized during the acquisition. Low-dose CT was acquired with Discovery IQ hybrid PET/CT scanner[36] (GE Healthcare) with the following parameters: 140 kVp; pitch, 0.94; collimation, 20 × 1.25 mm; reconstructed slice thickness, 3.75 mm; and increment, 3.26 mm. Emission data were corrected for randoms, dead time, scatter, and attenuation.

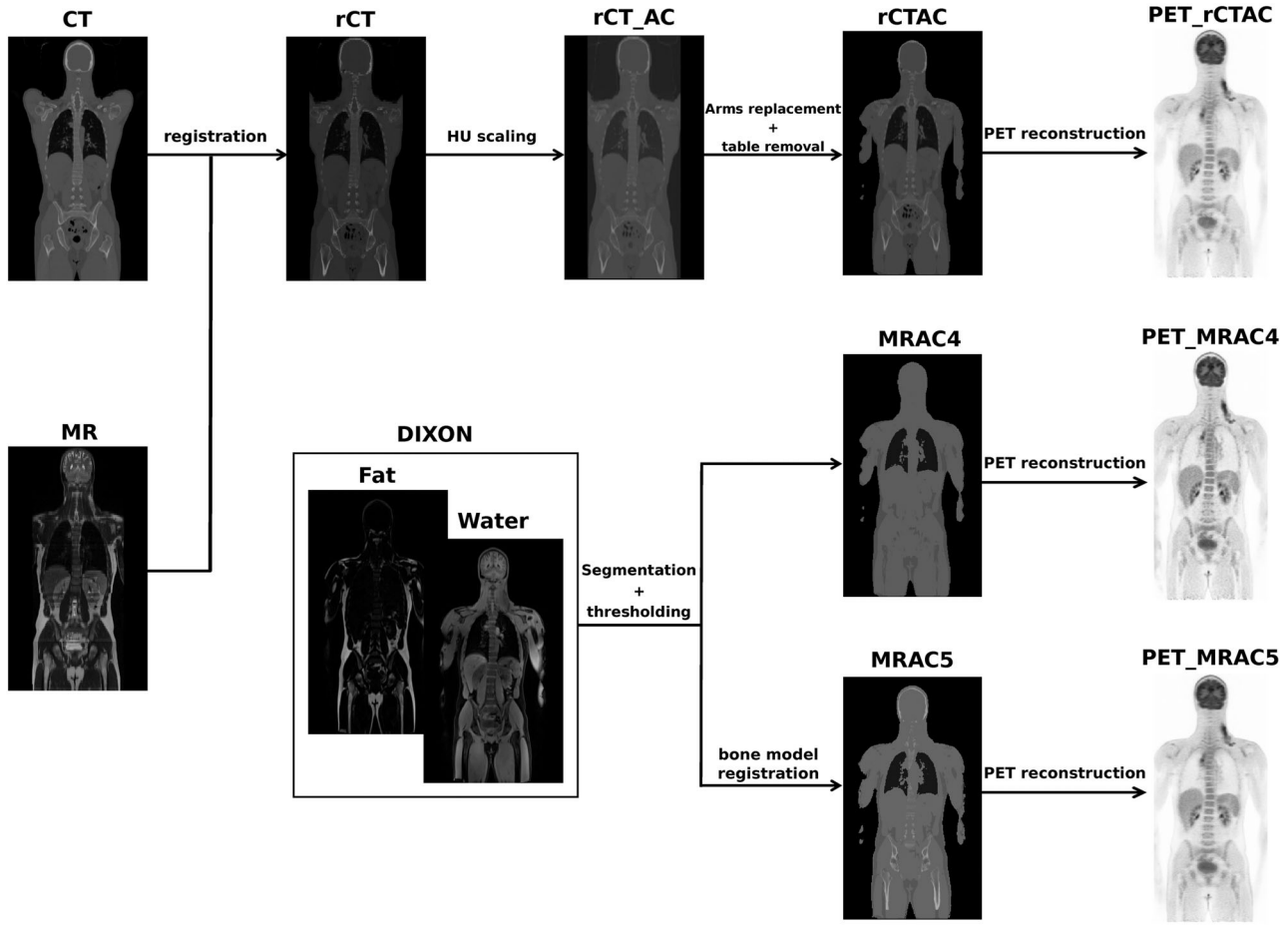

FIGURE 1 Overview of the workflow for reconstruction of PET images using CT-based attenuation correction (AC) map (PET_rCTAC), four-tissues MR-based AC maps, (PET_MRAC4), and five-tissues MR-based AC (PET_MRAC5). rCT images are the result of registration of CT on MR. rCT_AC represents rCT image converted to linear attenuation coefficients (LAC) values. MRAC4 and MRAC5 are the four-tissues and five-tissues MR-based AC maps, respectively. rCTAC is the resulting image after morphological operations

2.3 | PET/MR acquisition

Data were acquired on a 3T Siemens Biograph mMR hybrid PET/MR system[37] (Erlangen, version VE11) after the PET/CT scan. PET images were acquired simultaneously with a whole-body MRI T2 HASTE sequence (TR, 1400; TE, 87; slice thickness, 6 mm; and field of view, 380 × 380) and a Dixon MRI sequence (first TE, 1.23 ms; second TE, 2.46 ms; TR, 3.96 ms; voxel size, 4.1 × 2.6 × 3.1 mm; field of view, 500 × 312; and zoom factor 1.0). PET required 5 min per bed position, for a total time of 25 min of PET acquisition. Matrix size of PET was 172 × 172 × 515, resulting in a voxel size of 4.1 × 4.1 × 2.0.

2.3.1 | MRAC maps generation

MRAC4 and MRAC5 maps were generated from the Dixon MR sequence using the dedicated tool for offline generation of attenuation maps available on the software platform (syngo MR E11P; Siemens Healthcare GmbH) of the scanner. MRAC4 map was generated with the *baseline segmentation method* implemented on Biograph mMR.[11] For the MRAC5 map, the method described by Paulus et al.[13] was used.

2.3.2 | rCTAC map generation

CT data from PET/CT scanner was used to derive a CT-based AC map (registered CTAC, denoted as rCTAC) following the procedure described in Figure 1 and detailed below.

Firstly, CT image was aligned to MR T2-weighted image by means of two-steps registration procedure both performed by using Elastix software (v. 4.9.0, http://elastix.isi.uu.nl/). Taking into account the multimodal strategy proposed by Leibfarth et al.[38] for the registration procedure, as first step a rigid registration was performed to achieve a rough alignment of the fixed and moving images. A four-level multiresolution approach

using a Gaussian smoothing without downsampling was applied. A localized version of mutual information was considered as similarity measure, consisting in evaluating mutual information on multiple subregions. Specifically, the localization is obtained by constraining the sampling procedure to a cubic subregion of the image, randomly chosen in every iteration step from the fixed image domain.[38,39] The standard gradient descent was applied for metric optimization.[40] The resulting transformation matrix was used to initialize the following deformable registration step. In particular, a three-level multiresolution approach using 3D Gaussian smoothing (sigma = 8.0, 4.0, and 1.0 in in-plane acquisition and sigma = 2.0, 1.0, and 1.0 in the third direction to take into account voxel anisotropy) without downsampling was used together with a bending energy penalty term calculated to regularize the transformation. Finally, the similarity metric consisted in a combination of localized mutual information and bending energy penalty (with 60 bins, 10 000 samples, and a maximum of 5000 iterations for each resolution) and the adaptive stochastic gradient descent optimizer was adopted for its minimization.[40] B-spline was used as interpolation method for the registration procedure.

After the registration step, the resulted image (rCT) was visually checked to confirm the consistency of structural alignment with MR image. Moreover, to support the qualitative evaluation of the registration performance, we generated mosaic images of MRAC and rCTAC for the entire patient population and performed quantitative comparison of rCTAC with both MRAC4 and MRAC5 by using the Dice similarity coefficient (DSC). In particular, the masks related to each tissue class were obtained as follows: for rCTAC, voxels in the range of 0.005–0.05 cm^{-1} were assigned to the lungs, voxels in the range of 0.05–0.093 cm^{-1} were assigned to fat, voxels over 0.093 cm^{-1} were all assigned to soft tissue for rCTAC-MRAC4 DSC analysis, while those over 0.105 cm^{-1} were assigned to bone tissue for rCTAC-MRAC5 DSC analysis.[11] For MRAC 4, lungs, fat and soft tissue corresponded to values equal to 0.022 cm^{-1}, 0.085 cm^{-1}, and 0.1 cm^{-1}. The same goes for MRAC5, with the difference that voxels greater than 0.100 were assigned to bone tissues.[13] Then, rCT was converted to LAC values by means of a piece-wise linear equation transformation,[10] thus resulting in rCT_AC map.

Since the obtained rCT_AC image anatomically differed from MRAC map for both arm positions (arms up in PET/CT acquisition, arms down in PET/MR acquisition) and table contribution in the attenuation values, an approach to make the attenuation maps comparable was adopted. In particular, the rCT_AC voxels from the relative complement of the foreground rCT_AC mask and the foreground MRAC mask (e.g., the ensemble of foreground voxels in rCTAC but not in MRAC) were automatically replaced with the corresponding voxel values from MRAC. The MRAC foreground binary mask was evaluated by selecting voxels with LAC greater than zero (LAC assigned to the outer air class) whereas the rCT_AC foreground mask was obtained by means of the Otsu thresholding method.[41] In addition to arms and table replacement, the latter approach automatically replaced missing LAC values in rCT_AC map arising from the different field of view (FOV) between MR and CT images after the registration procedure.

2.4 | PET data reconstruction

PET data acquired from PET/MR were corrected for random coincidences, dead time and scatter, as implemented on the PET/MR system. A 3D attenuation weighted ordered-subsets expectation maximization iterative reconstruction algorithm (AW OSEM 3D) with three iterations and 21 subsets, Gaussian smoothing 4 mm full width at half maximum, was used. PET data were corrected for attenuation using MRAC4, MRAC5, and rCTAC, resulting in PET_MRAC4 (where PET_MRAC is PET images reconstructed using MR-based attenuation correction map), PET_MRAC5, and PET_rCTAC (PET images reconstructed using CT-based attenuation correction map), respectively (Figure 1).

2.5 | Data analysis

SUVs were calculated on the basis of body weight[42,43]:

$$\mathrm{SUV} = \frac{\textit{Activity Concentration in ROI} \times \textit{body weight}}{\textit{Injected dose}}$$

Regions of interest (ROIs) were drawn in spinal cord (SC), lumbar cerebrospinal fluid (CSF), and vertebral body marrow on a T2-weighted image at five levels (C2, C5, T6, T12, and L3).

For each level, two fiducial points were manually drawn respectively on the spinal cord and the corresponding vertebral body bone marrow (lumbar CSF in case of L3 level), by selecting the best representative slice in axial orientation. Next, 3D ROIs were automatically generated, with a custom MATLAB routine, by centering a spherical ROI with diameter of 9 mm to each fiducial point. An example of the distribution of the 10 ROIs for one of the included patients is shown in Figure 2.

The generated ROIs were copied to PET_MRAC4, PET_MRAC5 and PET_rCTAC images and the average SUV (SUV_m) across all voxels, within each ROI, was computed from each reconstructed PET.

Then, the SUV_m across all voxels within each ROI was computed from PET_MRAC4, PET_MRAC5, and PET_rCTAC images.

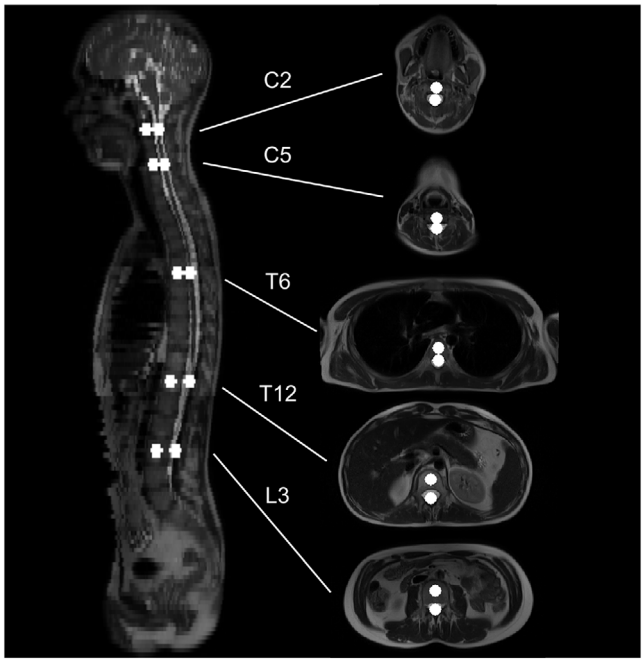

FIGURE 2 Distribution of the 10 3D regions of interest (ROIs) for one of the included patients. On the left, the sagittal view of a central slice overlapped by the sagittal MIP of segmentation mask. On the right, the five axial slices, each containing two ROIs (the central slice of each 3D ROI was shown). 3D ROIs were centered on the spinal cord and the corresponding vertebral body bone marrow (lumbar CSF in case of L3 level)

2.6 | Statistical analysis

Statistical analysis was performed using MATLAB R2020a.

For each ROI, two-tailed paired *t*-test was performed with a twofold aim: to compare SUV_m values arising from PET corrected for the two MRAC maps (respectively, SUV_{m_MRAC4} and SUV_{m_MRAC5}) and then to assess differences across the two MRAC methods and SUV_m from PET_rCTAC (SUV_{m_rCTAC}), the latter assumed as reference. The statistical significance level was set at $p < 0.05$. Then, Bonferroni correction was applied for minimizing type-I error ($p < 0.05/3 \rightarrow p < 0.0167$). In order to investigate the magnitude of the difference in SUVs between the two MRAC models, as well as that between each MRAC model and rCTAC, the effect size (ES) was calculated by means of Cohen's *d*, defined as follows[44]:

$$d = \frac{SUV_{m1\_avg} - SUV_{m2\_avg}}{SD_{pool}},$$

where SUV_{m1_avg} and SUV_{m2_avg} are the average SUV_m from the PET images reconstructed with two different AC methods (the methods compared against each other being MRAC4, MRAC5, and rCTAC), while SD_{pool} is the pooled standard deviation for SUV_{m1_avg} and SUV_{m2_avg}. ES was categorized as very small (<0.2), small (0.21–0.5), medium (0.51–0.8), large (0.81–1.2), very large (1.21–2), and huge (> 2).[45] In order to assess the consistency between AC models, the association between the MRAC4 and MRAC5, as well as that between each MRAC model and rCTAC was evaluated by Pearson's correlation (*r*) and interpreted as follows: poor correlation ($0.00 \leq r \leq 0.20$), fair correlation ($0.20 < r \leq 0.40$), moderate correlation ($0.40 < r \leq 0.60$), good correlation ($0.60 < r \leq 0.80$), and very good correlation ($r > 0.80$). Comparison of correlation coefficients of MRAC models with rCTAC was performed for each spinal zone using Meng's *z*-test.[46]

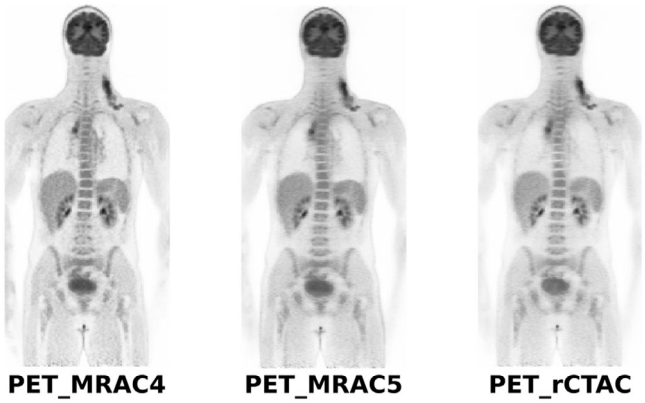

FIGURE 3 PET data reconstructed from MRAC4 (left), MRAC5 (center), and rCTAC (right) maps

3 | RESULTS

The visual inspection supported by mosaic images showed a consistent alignment between the MR and CT modalities (Figure S1). Results of DSC analysis are reported in Table S1.

In Figure 3, PET data reconstructed from both MRAC and rCTAC maps are shown.

For each ROI, the values of SUV_{m_MRAC5}, SUV_{m_MRAC4}, mean differences between the two, effect sizes, and *r* values are summarized in Table 1. SUV_{m_MRAC5} values were significantly higher than SUV_{m_MRAC4} in C2, C5, T6 SC, T12 SC, and L3 CSF. There is no proof of statistically significant differences in the remaining vertebral levels analyzed. These considerations could also be confirmed by observing values of effect size, which showed higher values ($0.24 < d < 0.95$) in the five abovementioned statistically significant zones with respect to the remaining ones ($0.08 < d < 0.14$). Interestingly, in L3 CSF, the comparison among the two MRAC methods yielded a very large effect size ($d = 0.95$). SUV_{m_MRAC4} and SUV_{m_MRAC5} showed very good correlation ($0.81 < r < 0.97$) in all spinal ROIs.

TABLE 1 Comparison between average standardized uptake value (SUV) arising from PET corrected from four-tissues MRAC (SUV_{m_MRAC4}) and average SUV arising from PET corrected from five-tissues MRAC (SUV_{m_MRAC5})

Level	SUV_{m_MRAC5} mean (range)	SUV_{m_MRAC4} mean (range)	MD (SD)	ES	*r*
C2	1.72 (0.76–3.61)	1.59 (0.67–3.21)	0.13 (0.13)*	0.24	0.93**
C2 SC	1.38 (0.9–2.18)	1.4 (0.89–2.11)	−0.02 (0.07)	0.08	0.94**
C5	1.96 (0.94–3.53)	1.78 (0.64–3.14)	0.17 (0.12)*	0.35	0.97**
C5 SC	1.55 (0.86–2.2)	1.52 (0.66–2.13)	0.03 (0.07)	0.1	0.95**
T6	2.31 (0.74–5.12)	2.28 (0.83–4.68)	0.03 (0.2)	0.03	0.93**
T6 SC	1.37 (0.56–2.29)	1.27 (0.61–2.16)	0.1 (0.08)*	0.28	0.86**
T12	2.21 (0.86–5.36)	2.16 (0.71–5.14)	0.05 (0.2)	0.06	0.96**
T12 SC	1.51 (0.95–2.79)	1.33 (0.82–2.63)	0.17 (0.09)*	0.45	0.85**
L3	2.19 (1.05–4.23)	2.31 (0.83–3.98)	−0.12 (0.19)	0.14	0.88**
L3 CSF	1.13 (0.68–1.95)	0.87 (0.47–1.58)	0.26 (0.06)*	0.95	0.81**

Abbreviations: ES, effect size; MD, mean difference.
*Statistically significant to paired *t*-test.
***r* significantly different from zero.

TABLE 2 Comparison between average standardized uptake value (SUV) arising from PET corrected from four- and vie-tissues MRAC (SUV_{m_MRAC4} and SUV_{m_MRAC5}), and SUV arising from PET corrected from CT-based attenuation correction (AC) map (SUV_{m_rCTAC})

Level	SUV_{m_rCTAC} mean (range)	MD (SD)		ES		*r*	
		$SUV_{m_{MRAC4}}$	SUV_{m_MRAC5}	SUV_{m_MRAC4}	SUV_{m_MRAC5}	SUV_{m_MRAC4}	SUV_{m_MRAC5}
C2	1.66 (0.44–3.41)	0.07 (0.15)	0.07 (0.14)	0.12	0.11	0.81**	0.77**
C2 SC	1.32 (0.73–2.08)	0.06 (0.07)*	0.08 (0.07)	0.26	0.19	0.9**	0.88**
C5	1.88 (0.88–3.34)	0.07 (0.12)	0.1 (0.12)	0.19	0.14	0.87**	0.89**
C5 SC	1.48 (0.73–2.22)	0.07 (0.07)	0.04 (0.07)*	0.13	0.23	0.89**	0.93**
T6	1.98 (0.6–4.85)	0.32 (0.2)*	0.3 (0.18)*	0.38	0.39	0.88**	0.94**
T6 SC	1.25 (0.45–2.08)	0.12 (0.09)	0.02 (0.08)*	0.06	0.32	0.84**	0.83**
T12	2.23 (0.87–4.89)	0.02 (0.21)	0.07 (0.21)	0.08	0.02	0.87**	0.83**
T12 SC	1.53 (0.83–3.08)	0.03 (0.11)	0.2 (0.11)	0.42	0.06	0.67**	0.8**
L3	2.17 (0.66–4.43)	0.02 (0.21)	0.14 (0.2)	0.16	0.02	0.78**	0.73**
L3 CSF	1.17 (0.62–2.83)	0.04 (0.09)*	0.3 (0.08)	0.83	0.11	0.67**	0.78**

Abbreviations: ES, effect size; MD, mean difference.
*Statistically significant to paired *t*-test performed against SUV_{m_rCTAC}.
***r* significantly different from zero.

Concerning the comparison between MRAC models and CTAC model (Table 2), SUV_{m_MRAC4} and SUV_{m_MRAC5} were both lower than SUV_{m_rCTAC} in all 10 ROIs. However, paired *t*-test revealed statistical significance only in C2 SC and L3 CSF for MRAC4, T6 SC and C5 SC for MRAC5, and T6 for both MRAC methods. Except for C5 SC, T6 SC and T6, the MRAC5 method yielded a lower effect size than MRAC4. As reported in Table 2, both SUV_{m_MRAC4} and SUV_{m_MRAC5} showed a good or very good correlation with SUV_{m_rCTAC} at each ROI level. SUV_{m_MRAC5} showed an overall higher correlation with SUV_{m_rCTAC}, although comparison of the latter with *r* between SUV_{m_MRAC4} and SUV_{m_rCTAC} was not significant in any of the 10 investigated zones according to Meng's *z*-test.

4 | DISCUSSION

In this study, we evaluated the influence of the MRAC methods implemented on the integrated PET/MR scanner (MRAC4 and MRAC5) on FDG uptake estimation in spine and spinal cord imaging. Specifically, we compared PET data corrected with MRAC methods with respect to those corrected with rCTAC and investigated the effect of including bone in MRAC4. rCTAC map was assumed as reference standard for the AC and used to retrospectively reconstruct PET/MR emission data. In fact, a direct comparison between PET/MR and PET/CT would not be properly suitable since the SUV comparison between different timepoints and scanners could be influenced by several factors related to technical and biological

issues due to different uptake time among PET/MR and PET/CT sessions.[47]

Since bone structures cause the highest attenuation in the body, we expected to find a significant underestimation of SUV from PET/MRI corrected with MRAC4 in regions surrounded by a high occurrence of bony structures such as the spine, with respect to PET_rCTAC. This SUV underestimation was expected to be less substantial when PET/MRI is corrected with MRAC5.

In fact, our findings show that the comparison among MRAC methods indicated that the absence of bone in MRAC4 map cannot be neglected since SUVs from PET_MRAC4 are overall lower than those from PET_MRAC5 and their differences were statistically significant at five levels (C2, C5, T6 SC, T12 SC, L3 CSF). Interestingly, adding bone at lower spinal levels yielded a higher effect size (d = 0.45 at T12 SC, d = 0.95 at L3 CSF), and this could be attributed to the higher bone presence at these levels, in particular in the pelvis region.[31]

The expected SUVs underestimations between PET_MRAC4 and PET_rCTAC were confirmed by results obtained, showing SUVs underestimation at all 10 investigated levels, with statistically significant differences at C2, T6, and L3 CSF. Although SUVs underestimation and statistically significant differences persisted even when considering PET correction for MRAC5 with respect to the reference, an overall decrease in effect size could be observed, mainly at lower spinal levels (T12, L3).

In summary, our results indicate that the differences between investigated AC methods are also sensitive to the ROI localization, in particular to both the structure (bone marrow or spinal cord) and the related spinal level.

While similar studies focused on the comparison between MRAC with CTAC by analyzing PET images acquired with different scanners[10,22–28] (e.g., PET/CT scanner and PET/MR scanner), to our knowledge, this is the first study evaluating the impact of the MRAC on the spinal cord PET/MR imaging, investigating also the effect of including bones with five-compartment attenuation maps and assuming a CT-driven map as reference for the AC.

Two previous studies compared CT-driven and four-tissues MR-driven AC on the FDG-PET data acquired on a PET/MR scanner[48,49] on different anatomical districts. In both studies, variable percentage differences between CT-driven and MR-driven mean SUV values, depending on examined body regions, were found. Seith et al.[48] quantified SUV mean in different body regions considering normal and injured soft tissues, as well as normal bone and bone lesions, and confirmed the expected higher underestimation of mean SUV in bones assessed with MR-driven AC methods not accounting for bones. This was also confirmed in the study of Arabi et al.[50] who compared three- and four-tissues MRAC with AC derived from CT images in terms of accuracy of SUV quantification and found highest underestimations of MRAC models in bony regions.

In a recent study, Liu et al.[49] also used a CT-derived approach analogous to that developed in the present study, finding underestimations in SUV mean between MRAC4 and CT-driven methods for normal and injured soft tissues. Underestimations increased for normal bone and bone lesions. Similar to our results, they also found a very high Pearson's correlation between the two AC methods, either in soft or bone tissues ($0.93 < r < 0.99$).

Overall, underestimation of mean SUV values using MRAC4 with respect to CT-driven AC method also appeared in our findings, mainly at pelvis level.

Few recent studies investigated the impact of five-tissues MRAC in whole-body PET/MR evaluation.[13,31–33] Paulus et al.,[13] using CTAC from PET/CT as reference standard, found that five-tissues MRAC improves SUV quantification in whole-body hybrid PET/MR imaging, especially in bony tissue and nearby soft tissue. Similarly, Domacevsky et al.[31] evaluated the impact of using five-tissues MRAC in ^{68}Ga-PSMA-11 PET/MR of prostate cancer patients with respect to four-tissues MRAC and using CTAC from PET/CT as reference standard, finding that the addition of bones to the four-tissue MRAC model has an impact on SUV measurements. We also noticed a non-negligible impact on SUV measurements arising from the addition of bone in MRAC4, although a direct comparison with mentioned studies cannot be performed due to different methods, investigated zones, and reference standard. Oehmigen et al.[33] also found significant differences between SUV measurements based on MRAC4 and MRAC5 methods in bone lesions, but no CT-based reference standard was used.

In the present study, the analyzed population consisted in patients with oncological complications, selected based on the absence of lesions within the spine and the spinal cord. Our choice was motivated by the intention of investigating the role of PET/MR imaging for the study of neurological diseases involving spinal cord. Among these we might mention the evaluation of inflammatory myelopathies (e.g., multiple sclerosis), neurosarcoidosis, amyotrophic lateral sclerosis (ALS), trauma, post radiation myelopathy, and some neurodegenerative diseases affecting the SC.[23,51–56] The evaluation of the reliability of FDG-PET/MR imaging therefore becomes fundamental for this type of pathologies for which small variations of the radiotracer in the spinal cord must be appreciable. For example, spinal onset of ALS was associated with a slight significant increase in SC uptake of FDG, thus reflecting an increased metabolism of SC structures.[55] Previous studies[30,35] investigated the influence of MRAC in spine lesions finding a substantial underestimation of SUV values with respect to CTAC. However, their findings are not based on the data obtained from the acquired MR

images since the AC map was derived by simulating the attenuation values from the CT image. Further studies are required to specifically investigate the influence of AC map calculated from the PET/MR system also in lesions located both in spine and spinal cord.

Our study has several limitations. First of all, the assumption of rCTAC method as reference implies sensitivity to registration errors that may have occurred in registration of CT to MR images[57] and may have affected SUV measurements. However, the alignment between registered modalities has been carefully checked by visual examination, and residual misalignments were not considered to be a relevant source of bias. In addition, the reported DSC between rCTAC and both MRAC4 and MRAC5 tissue classes was overall high, except for bone tissue. However, this could be justified by another source of bias related to the missing bone information in the MRAC5 bone model with respect to rCTAC (e.g., ribs, bones at shoulder level).[13] Moreover, according to the issue recently raised by Bogdanovic et al.,[58] our reported results, concerning the comparison of SUV between MRAC4 and MRAC5, could be affected by possible bone misregistration with bone-atlas template.[13] Then, it should be considered that the patients' arms in rCTAC were replaced by the corresponding MRAC segmented arms, which did not contain bone structures. This can lead to a potential slight misinterpretation of PET in the shoulder zone.[48] However, due to the existing distance between shoulders and spine, the spinal regions should not be affected by such biases. Moreover, the different arm position between the two modalities could also have led to biased registration results. However, since the registration procedure was based on the localized version of MI (which allows calculating a coregistration matrix with a greater local weight) the different arm position between MR and CT poorly influenced the coregistration result. Finally, it is worth noting that atlas-based methods for MRAC map generation may produce different results in studies with a narrower FOV (chest, cardiac imaging).[59–62] In this case, it would be advisable to develop specific studies for assessing the extensibility of our results to these applications.

5 | CONCLUSION

Our results show that neglecting bones in AC, as for the case of MRAC4, can produce an underestimation of the actual FDG uptake of the spinal cord. The inclusion of bone in MRAC5 improves the AC in spinal cord, although further investigations are needed to validate its use in clinical practice. Therefore, particular care must be taken in the spinal canal region and the use of AC maps that include the contribution of bone structures to the attenuation could be beneficial. In this context, the suitability of PET/MR imaging of spinal cord and bone marrow requires particular attention if quantitative estimations are required.

ACKNOWLEDGMENT

This work was supported by "Ricerca Corrente" Grant from Italian Ministry of Health (IRCCS SDN).

CONFLICT OF INTEREST

The authors declare no conflict of interest.

DATA AVAILABILITY STATEMENT

The datasets used and/or analyzed during the current study are available from the corresponding author on reasonable request.

REFERENCES

1. Thorwarth D, Leibfarth S, Mönnich D. Potential role of PET/MRI in radiotherapy treatment planning. *Clin Transl Imaging*. 2013;1(1):45-51.
2. Winter RM, Leibfarth S, Schmidt H, et al. Assessment of image quality of a radiotherapy-specific hardware solution for PET/MRI in head and neck cancer patients. *Radiother Oncol*. 2018;128(3):485-491.
3. Miller-Thomas MM, Benzinger TLS. Neurologic applications of PET/MR imaging. *Magn Reson Imaging Clin N Am*. 2017;25(2):297-313.
4. Uchida K, Nakajima H, Okazawa H, et al. Clinical significance of MRI/18F-FDG PET fusion imaging of the spinal cord in patients with cervical compressive myelopathy. *Eur J Nucl Med Mol Imaging*. 2012;39(10):1528-1537.
5. Nakamura Y, Liu Z, Fukumoto S, et al. Spinal cord involvement by atrophy and associations with disability are different between multiple sclerosis and neuromyelitis optica spectrum disorder. *Eur J Neurol*. 2020;27(1):92-99.
6. Bolcaen J, Acou M, Mertens K, et al. Structural and metabolic features of two different variants of multiple sclerosis: a PET/MRI study. *J Neuroimaging*. 2013;23(3):431-436.
7. Marini C, Morbelli S, Cistaro A, et al. Interplay between spinal cord and cerebral cortex metabolism in amyotrophic lateral sclerosis. *Brain*. 2018;141(8):2272-2279.
8. Izquierdo-Garcia D, Catana C. MR imaging–guided attenuation correction of PET data in PET/MR imaging. *PET Clinics*. 2016;11(2):129-149.
9. Catana C, Quick HH, Zaidi H. Current commercial techniques for MRI-guided attenuation correction are insufficient and will limit the wider acceptance of PET/MRI technology in the clinic. *Med Phys*. 2018;45(9):4007-4010.
10. Carney JPJ, Townsend DW, Rappoport V, Bendriem B. Method for transforming CT images for attenuation correction in PET/CT imaging: transforming CT images for attenuation correction in PET/CT. *Med Phys*. 2006;33(4):976-983.
11. Martinez-Moller A, Souvatzoglou M, Delso G, et al. Tissue classification as a potential approach for attenuation correction in whole-body PET/MRI: evaluation with PET/CT data. *J Nucl Med*. 2009;50(4):520-526.
12. Hofmann M, Pichler B, Schölkopf B, Beyer T. Towards quantitative PET/MRI: a review of MR-based attenuation correction techniques. *Eur J Nucl Med Mol Imaging*. 2009;36(S1):93-104.
13. Paulus DH, Quick HH, Geppert C, et al. Whole-body PET/MR imaging: quantitative evaluation of a novel model-based MR attenuation correction method including bone. *J Nucl Med*. 2015;56(7):1061-1066.
14. Su Y, Rubin BB, McConathy J, et al. Impact of MR-based attenuation correction on neurologic PET studies. *J Nucl Med*. 2016;57(6):913-917.

15. Werner P, Rullmann M, Bresch A, et al. Impact of attenuation correction on clinical [18F]FDG brain PET in combined PET/MRI. *EJNMMI Res*. 2016;6(1):47.
16. Øen SK, Keil TM, Berntsen EM, Aanerud JF, Schwarzlmüller T, Ladefoged CN, et al. Quantitative and clinical impact of MRI-based attenuation correction methods in [18F]FDG evaluation of dementia. *EJNMMI Res*. 2019;9(1):83.
17. Ladefoged CN, Law I, Anazodo U, et al. A multi-centre evaluation of eleven clinically feasible brain PET/MRI attenuation correction techniques using a large cohort of patients. *Neuroimage*. 2017;147:346-359.
18. Teuho J, Torrado-Carvajal A, Herzog H, et al. Magnetic resonance-based attenuation correction and scatter correction in neurological positron emission tomography/magnetic resonance imaging—current status with emerging applications. *Front Phys*. 2020;7:243.
19. Andersen FL, Ladefoged CN, Beyer T, et al. Combined PET/MR imaging in neurology: MR-based attenuation correction implies a strong spatial bias when ignoring bone. *Neuroimage*. 2014;84:206-216.
20. Pace L, Nicolai E, Aiello M, Catalano O, Salvatore M. Whole-body PET/MRI in oncology: current status and clinical applications. *Clin Transl Imaging*. 2013;1(1):31-44.
21. Nensa F, Beiderwellen K, Heusch P, Wetter A. Clinical applications of PET/MRI: current status and future perspectives. *Diagn Interv Radiol*. 2014;20(5):438-447.
22. Bezrukov I, Schmidt H, Mantlik F, et al. MR-based attenuation correction methods for improved PET quantification in lesions within bone and susceptibility artifact regions. *J Nucl Med*. 2013;54(10):1768-1774.
23. Aiello M, Alfano V, Salvatore E, et al. [18F]FDG uptake of the normal spinal cord in PET/MR imaging: comparison with PET/CT imaging. *EJNMMI Res*. 2020;10(1):91.
24. Eiber M, Takei T, Souvatzoglou M, et al. Performance of whole-body integrated 18F-FDG PET/MR in comparison to PET/CT for evaluation of malignant bone lesions. *J Nucl Med*. 2014;55(2):191-197.
25. Heusch P, Buchbender C, Beiderwellen K, et al. Standardized uptake values for [18F] FDG in normal organ tissues: comparison of whole-body PET/CT and PET/MRI. *Eur J Radiol*. 2013;82(5):870-876.
26. Drzezga A, Souvatzoglou M, Eiber M, et al. First clinical experience with integrated whole-body PET/MR: comparison to PET/CT in patients with oncologic diagnoses. *J Nucl Med*. 2012;53(6):845-855.
27. Seith F, Schmidt H, Gatidis S, et al. SUV-quantification of physiological lung tissue in an integrated PET/MR-system: impact of lung density and bone tissue. *PLoS One*. 2017;12(5):e0177856.
28. Aznar MC, Sersar R, Saabye J, et al. Whole-body PET/MRI: the effect of bone attenuation during MR-based attenuation correction in oncology imaging. *Eur J Radiol*. 2014;83(7):1177-1183.
29. Schulz V, Torres-Espallardo I, Renisch S, et al. Automatic, three-segment, MR-based attenuation correction for whole-body PET/MR data. *Eur J Nucl Med Mol Imaging*. 2011;38(1):138-152.
30. Samarin A, Burger C, Wollenweber SD, et al. PET/MR imaging of bone lesions—implications for PET quantification from imperfect attenuation correction. *Eur J Nucl Med Mol Imaging*. 2012;39(7):1154-1160.
31. Domachevsky L, Goldberg N, Gorenberg M, Bernstine H, Groshar D, Catalano OA. Prostate cancer evaluation using PET quantification in 68Ga-PSMA-11 PET/MR with attenuation correction of bones as a fifth compartment. *Quant Imaging Med Surg*. 2020;10(1):40-47.
32. Elschot M, Selnæs KM, Johansen H, Krüger-Stokke B, Bertilsson H, Bathen TF. The effect of including bone in dixon-based attenuation correction for ^{18} F-fluciclovine PET/MRI of prostate cancer. *J Nucl Med*. 2018;59(12):1913-1917.
33. Oehmigen M, Lindemann ME, Gratz M, et al. Impact of improved attenuation correction featuring a bone atlas and truncation correction on PET quantification in whole-body PET/MR. *Eur J Nucl Med Mol Imaging*. 2018;45(4):642-653.
34. Keereman V, Van Holen R, Mollet P, Vandenberghe S. The effect of errors in segmented attenuation maps on PET quantification: PET quantification with segmented attenuation maps. *Med Phys*. 2011;38(11):6010-6019.
35. Kim JH, Lee JS, Song I-C, Lee DS. Comparison of segmentation-based attenuation correction methods for PET/MRI: evaluation of bone and liver standardized uptake value with oncologic PET/CT data. *J Nucl Med*. 2012;53(12):1878-1882.
36. Reynés-Llompart G, Gámez-Cenzano C, Romero-Zayas I, Rodríguez-Bel L, Vercher-Conejero JL, Martí-Climent JM. Performance characteristics of the whole-body discovery IQ PET/CT system. *J Nucl Med*. 2017;58(7):1155-1161.
37. Delso G, Furst S, Jakoby B, et al. Performance measurements of the Siemens mMR integrated whole-body PET/MR scanner. *J Nucl Med*. 2011;52(12):1914-1922.
38. Leibfarth S, Mönnich D, Welz S, et al. A strategy for multimodal deformable image registration to integrate PET/MR into radiotherapy treatment planning. *Acta Oncol*. 2013;52(7):1353-1359.
39. Klein S, van der Heide UA, Lips IM, van Vulpen M, Staring M, Pluim JPW. Automatic segmentation of the prostate in 3D MR images by atlas matching using localized mutual information: automatic segmentation of the prostate in MR images. *Med Phys*. 2008;35(4):1407-1417.
40. Klein S, Staring M, Andersson P, Pluim JPW. Preconditioned stochastic gradient descent optimisation for monomodal image registration. In: Fichtinger G, Martel A, Peters T, eds. *Medical Image Computing and Computer-Assisted Intervention – MICCAI 2011*. Springer; 2011:549-556.
41. Otsu N. A threshold selection method from gray-level histograms. *IEEE Trans Syst, Man, Cybern*. 1979;9(1):62-66.
42. Soongsathitanon S, Masa-Ah PM-AP, Tuntawiroon MTM. A new standard uptake values (SUV) calculation based on pixel intensity values. *Int J Math and Comput Simul*. 2012;6(1):26–33.
43. Masa-Ah P, Soongsathitanon S. A novel Standardized Uptake Value (SUV) calculation of PET DICOM files using MATLAB. 4.
44. Cohen J. *Statistical Power Analysis for the Behavioral Sciences*. Rev. ed. Academic Press; 1977.
45. Sawilowsky SS. New effect size rules of thumb. *J Mod App Stat Meth*. 2009;8(2):597-599.
46. Meng X, Rosenthal R, Rubin DB. Comparing correlated correlation coefficients. *Psychol Bull*. 1992;111(1):172-175.
47. Adams MC, Turkington TG, Wilson JM, Wong TZ. A systematic review of the factors affecting accuracy of SUV measurements. *Am J Roentgenol*. 2010;195(2):310-320.
48. Seith F, Gatidis S, Schmidt H, et al. Comparison of positron emission tomography quantification using magnetic resonance–and computed tomography–based attenuation correction in physiological tissues and lesions: a whole-body positron emission tomography/magnetic resonance study in 66 patients. *Invest Radiol*. 2016;51(1):66-71.
49. Liu G, Cao T, Hu L, et al. Validation of MR-based attenuation correction of a newly released whole-body simultaneous PET/MR system. *Biomed Res Int*. 2019;2019:1-10.
50. Arabi H, Rager O, Alem A, Varoquaux A, Becker M, Zaidi H. Clinical assessment of MR-guided 3-class and 4-class attenuation correction in PET/MR. *Mol Imaging Biol*. 2015;17(2):264-276.
51. Tomura N, Ito Y, Matsuoka H, et al. PET findings of intramedullary tumors of the spinal cord using [^{18} F] FDG and [^{11} C] methionine. *AJNR Am J Neuroradiol*. 2013;34(6):1278-1283.
52. Flanagan EP, Hunt CH, Lowe V, et al. [18F]-fluorodeoxyglucose–positron emission tomography in patients with active myelopathy. *Mayo Clin Proc*. 2013;88(11):1204-1212.

53. Ayrignac X, Orgeval J, Mariano-Goulart D. Sensitivity of [18F]-fluorodeoxyglucose–positron emission tomography in patients with active myelopathy. *Mayo Clin Proc*. 2014;89(6):859.
54. Kiamanesh Z, Banezhad F, Nasiri Z, Emami F, Treglia G, Sadeghi R. Physiological distribution of ^{18} F-FDG in the spinal cord: a systematic review. *J Spinal Cord Med*. 2021;44(4):517-524.
55. Marini C, Cistaro A, Campi C, et al. A PET/CT approach to spinal cord metabolism in amyotrophic lateral sclerosis. *Eur J Nucl Med Mol Imaging*. 2016;43(11):2061-2071.
56. Yamashita T, Hatakeyama T, Sato K, et al. Hypoxic stress visualized in the cervical spinal cord of ALS patients. *Neurol Res*. 2021;43(6):429-433.
57. van Velden FH, van Beers P, Nuyts J, et al. Effects of rigid and non-rigid image registration on test-retest variability of quantitative [18F]FDG PET/CT studies. *EJNMMI Res*. 2012;2(1):10.
58. Bogdanovic B, Gafita A, Schachoff S, et al. Almost 10 years of PET/MR attenuation correction: the effect on lesion quantification with PSMA: clinical evaluation on 200 prostate cancer patients. *Eur J Nucl Med Mol Imaging*. 2021;48(2):543-553.
59. Lau JMC, Laforest R, Sotoudeh H, et al. Evaluation of attenuation correction in cardiac PET using PET/MR. *J Nucl Cardiol*. 2017;24(3):839-846.
60. Thomas BA, Molton JS, Leek F, et al. A comparison of 18F-FDG PET/MR with PET/CT in pulmonary tuberculosis. *Nucl Med Commun*. 2017;38(11):971-978.
61. Rauscher I, Eiber M, Furst S, et al. PET/MR imaging in the detection and characterization of pulmonary lesions: technical and diagnostic evaluation in comparison to PET/CT. *J Nucl Med*. 2014;55(5):724-729.
62. Vontobel J, Liga R, Possner M, et al. MR-based attenuation correction for cardiac FDG PET on a hybrid PET/MRI scanner: comparison with standard CT attenuation correction. *Eur J Nucl Med Mol Imaging*. 2015;42(10):1574-1580.

SUPPORTING INFORMATION

Additional supporting information may be found online in the Supporting Information section at the end of the article.

How to cite this article: Brancato V, Borrelli P, Alfano V, et al. The impact of MR-based attenuation correction in spinal cord FDG-PET/MR imaging for neurological studies. *Med Phys*. 2021;48:5924–5934. https://doi.org/10.1002/mp.15149